Rapid synthesis of photoactive hydrogenated TiO$_2$ nanoplumes

Viviana Scuderi [a], Giuliana Impellizzeri [a,*], Massimo Zimbone [a], Ruy Sanz [a], Alessandro Di Mauro [a], Maria Antonietta Buccheri [a], Maria Miritello [a], Antonio Terrasi [a,b], Giancarlo Rappazzo [c], Giuseppe Nicotra [d], Vittorio Privitera [a]

[a] CNR-IMM, Via S. Sofia 64, 95123 Catania, Italy
[b] Department of Physics and Astronomy, University of Catania, Via S. Sofia 64, 95123 Catania, Italy
[c] Department of Biological, Geological and Environmental Sciences, University of Catania, Via Androne 81, 95124 Catania, Italy
[d] CNR-IMM, Z.I. VIII Strada 5, Catania 95121, Italy

ABSTRACT

In this study we employed hydrogen peroxide etching of Ti films as a straightforward method to synthesize hydrogenated TiO$_2$ nanoplumes. The material was extensively characterized, showing, among other special features, the inclusion of OH groups. These groups together with the generated structural defects and the nanostructuration are crucial for the high photocatalytic properties under ultraviolet (UV) and visible (VIS) light irradiation. In particular, nanoplumes show a reaction rate about 5 times the rate of TiO$_2$ flat films. Furthermore, nanoplumes display a significant antibacterial activity under VIS light irradiation, compared with TiO$_2$ films.

© 2015 Elsevier B.V. All rights reserved.

1. Introduction

Titanium dioxide, commonly called titania, plays a central role in energy and environmental research, finding applications in dye-sensitized solar cells, in lithium ion batteries, as photocatalyst for hydrogen production by water splitting, in self-cleaning coatings, and as photocatalyst for water treatment [1–7].

However, the TiO$_2$ photocatalytic efficiency is limited by its wide band-gap energy ($\sim$3 eV), which limits the spectrum of photons that can create electron–hole pairs to the ultraviolet (UV) light [8]. The methods to enhance the photocatalytic properties of TiO$_2$ are mainly based on the inhibition of the photo-generated electrons–holes recombination, on the increase of the exposed surface area, and on the decrease of the TiO$_2$ band-gap energy [9–14].

Recently, black hydrogenated TiO$_2$ has received extensive interest, and it is considered to have a great potential due to its extremely-enhanced absorption in the visible (VIS) and infrared (IR) region. However, the role of the hydrogenation in the enhanced photoactivity of TiO$_2$ is still ambiguous and different possible explanations have been given, such as the role of the surface disorder, the presence of Ti–OH or Ti–H surface bonds, the synergistic presence of oxygen vacancies and the surface disorder [15–19]. The synthesis of hydrogenated titania usually involves commercial Degussa P25 TiO$_2$ or titania nanorods and nanotubes [15–17,20]. The hydrogenation is always carried out in a tube furnace, with a temperature in the range of 200–550 °C, in a high-pressure H$_2$ atmosphere (up to 20 bar), and for a time from 3 h to 5 days.

In 2004 and 2009, hydrogen peroxide was used to oxidize metal titanium foils to prepare crystalline TiO$_2$ nanorods, and meso-porous TiO$_2$ films [21,22]. Tengvall et al. studied the titanium peroxide gels derived from the interaction between metallic Ti and H$_2$O$_2$, trying to clarify the biocompatibility of titanium [23]. Subsequent thermal treatments (at 473 K in Ar ambient) caused a rapid decomposition of the titania gel, forming a blue-gray powder consisting in a mixture of rutile and anatase TiO$_2$ [24]. However, the final morphology and properties of the etched material, the choice of the temperature and hydrogen peroxide concentration, depend strictly on the physical–chemical structure of the film, because the etching could take place at the localized defects in the material.

In this study, we employed hydrogen peroxide etching of Ti films as a easy, rapid, and low-cost method to synthesize hydrogenated TiO$_2$ nanoplumes with significant photocatalytic properties under UV and VIS light irradiation. This TiO$_2$ nanostructure is, to our knowledge, totally original. Indeed, there is in literature only one work reporting on silver oxide nanoplumes [25]. An accurate characterization of the synthesized material was performed

by scanning electron microscopy (SEM), transmission electron microscopy in scanning mode (STEM), electron energy loss spectroscopy (EELS), energy-dispersive X-ray spectroscopy (EDS), X-ray diffraction (XRD) measurements, X-ray Fourier transform infrared spectroscopy (FTIR), photoelectron spectroscopy (XPS), and UV–VIS optical characterization. Special attention was paid to the photocatalytic response of the material in the degradation of the Methylene Blue (MB) both under UV and VIS light irradiation. The antibacterial activity was tested on *Escherichia coli*, a well-known Gram-negative bacterium considered to be an indicator of fecal contamination in drinking water.

2. Materials and methods

2.1. Preparation

Titanium films, with a thickness of ~430 nm, were sputtered on quartz substrates by ultra-high vacuum magnetron sputtering technique from a Ti target of 99.99% purity. The Ti samples (1 cm × 1 cm in size) were put into 3 ml H_2O_2 (30%) solution at 60 °C for 190 s. The pH of the starting solution was measured to be 2.7. Afterwards, the samples were rinsed with deionized water and dried in air. Some samples were annealed in a conventional horizontal furnace at 400 °C for 1 h in a controlled oxygen ambient. TiO_2 flat film were synthesized by atomic layer deposition (ALD). The ALD was performed with a Picosun *R*-200 Advanced system, using $TiCl_4$ and de-ionized water as precursors, at a deposition temperature of 200 °C. Nitrogen (>99.999%) was used as carrier gas. The film thickness (~100 nm) was evaluated by the M-2000 spectroscopic ellipsometer by Woollam. This film was used as reference sample together with the sputtered Ti film.

2.2. Methods

SEM analyses in plan-view were performed by a field emission Zeiss Supra 25 microscope. TEM analyses were performed in cross-view with a JEOL JEM ARM200CF in scanning mode (STEM) at 60 kV of beam acceleration voltage using the microscope installed at Beyond–Nano Lab in Catania (Italy). This consists of a probe corrected STEM microscope equipped with a C-FEG with 0.27 eV energy spread, a 100 mm² silicon drift detector (SDD) on JEOL EDS with an energy resolution of 127 eV, and a fully loaded GATAN GIF Quantum ER as EELS spectrometer. This particular installation is capable to deliver a probe size of 1.1 Å at 60 kV. The low energy was used in order to reduce the specimen beam damage during the observation. All the EDS spectra, low- and core-loss EELS spectra were nearly simultaneously acquired, pixel by pixel, using the dual EELS capability, and stored in a data cube, in such a way the chemical maps may be reconstructed just by selecting the corresponding energy loss features stored in each pixel thanks to a technique called spectrum imaging (SI) [26].

XRD measurements were acquired by Bruker D-500 diffractometer at an incidence angle of 0.8°, and θ–2θ from 20 to 60°. Acquired spectrum were analyzed by Bruker software suite, including ICSD structure database.

XPS spectra were obtained using an AlKα photon source (1486.6 eV) and a hemispherical electron analyzer (VG CLAM4) in the integrated angle mode. All spectra were recorded at ~85° take-off angle, with an overall energy resolution of ~1 eV. Binding energies were calibrated setting the adventitious C 1s peak at 285 eV. The data were analyzed by the software XPSPEAK 4.1.

IR spectra were measured by Fourier transformed infrared PerkinElmer 1000 spectrophotometer operating in the range 1000–6000 cm⁻¹ with a resolution of 6 cm⁻¹. The IR measurements were performed under ambient conditions.

The optical characterization was obtained by extracting both the total transmittance (*T*) and the total reflectance (*R*) spectra in the 250–1100 nm wavelength range, by using a spectrophotometer (Lamda 35, PerkinElmer) equipped with an integrating sphere (RSA-PE-20,PerkinElmer).

The photocatalytic properties of the synthesized material were evaluated by the degradation of methylene blue, a chemical compound commonly used to evaluate the photocatalytic efficiency of a material. The experimental setup was in agreement with the ISO 10678:2010 international standard. The samples were immersed in a solution (2 ml) containing MB and de-ionized water (starting concentration: 1.3×10^{-5} M). The mixture was irradiated by an UV lamp (350–400 nm wavelength range) with a power of 8 W, or by a VIS lamp (420–520 nm wavelength range) with a power of 12 W, for a total time of 3 h. Every 30 min of irradiation the solutions were measured with an UV–VIS spectrophotometer (PerkinElmer Lambda 45) in 500–800 nm wavelength range. The degradation of MB was evaluated by the absorbance peak at 664 nm, according to the Lambert–Beer law. The decomposition of the dye in absence of any material was also checked as a reference. Before each measurement, the samples were irradiated by the UV lamp for 50 min in order to remove the hydrocarbons localized on the sample surface [27].

Antibacterial activity was tested on *E. coli* ATCC25922 strain. Bacteria were routinely maintained by spreading on McConkey agar. To run tests, a single colony was inoculated in 50 ml of Luria–Bertani (LB) broth and grown overnight at 37 °C by constant agitation at 180 rpm under aerobic conditions. The following day, the bacterial growth was measured by optical density at 600 nm. Bacteria were diluted up to 10^6 CFU/ml in phosphate buffer saline (PBS) and 100 μl were added onto the titania samples. Untreated bacteria and bacteria exposed to VIS only were run in parallel as controls. VIS source to induce photo-catalysis was the same as for MB degradation analysis. Aliquots were collected at 15 and 60 min, conveniently diluted by serial dilutions 1:10 and plated in LB Agar Petri dishes. Plates were incubated overnight at 37 °C. CFU were counted the following day. Experiments were made in triplicates.

3. Results and discussion

Fig. 1(a) and (b) show, respectively, two SEM images in plan-view of Ti film before and after the chemical etching in H_2O_2. Titanium film deposited by sputtering show a characteristic granular structure, responsible for the irregular shape of the surface (Fig. 1(a)). After the treatment in H_2O_2 the samples appear dark in color, and the porosity of the materials is enhanced, as revealed by the microscopy reported in Fig. 1(b).

Cross-view STEM images of Ti film acquired after the chemical etching in H_2O_2 (Fig. 1(c) and (d)) show the presence of a nanostructured material, ~300 nm in thickness, composed of porous quasi–columnar nanostructure. This structure recalls plumes, thus we called it nanoplumes. The high porosity of the nanoplumes suggests that the dissolution of the material was heterogeneous, possibly through localized defects, rather than uniform on the whole surface. At the bottom of the nanoplumes a residual Ti film, ~70 nm in thickness, is still visible (see Fig. 1(c)). Quantitative EDS analysis performed on the plumes through STEM, reported an atomic% concentration of 33.5 ± 2.1 and 66.5 ± 5.5 for titanium and oxygen, respectively, thus confirming the presence of TiO_2. An atomic concentration of 100% Ti was found on the residual Ti layer. The corresponding chemical map, reported in Fig. 1(e), clearly confirms the presence of O and Ti just in correspondence of the nanoplumes. This map was acquired through EELS spectrum imaging by selecting the Ti $L_{2,3}$ ionization edge, and the O K_1 ionization edge. We used EELS spectroscopy since the signal is much more
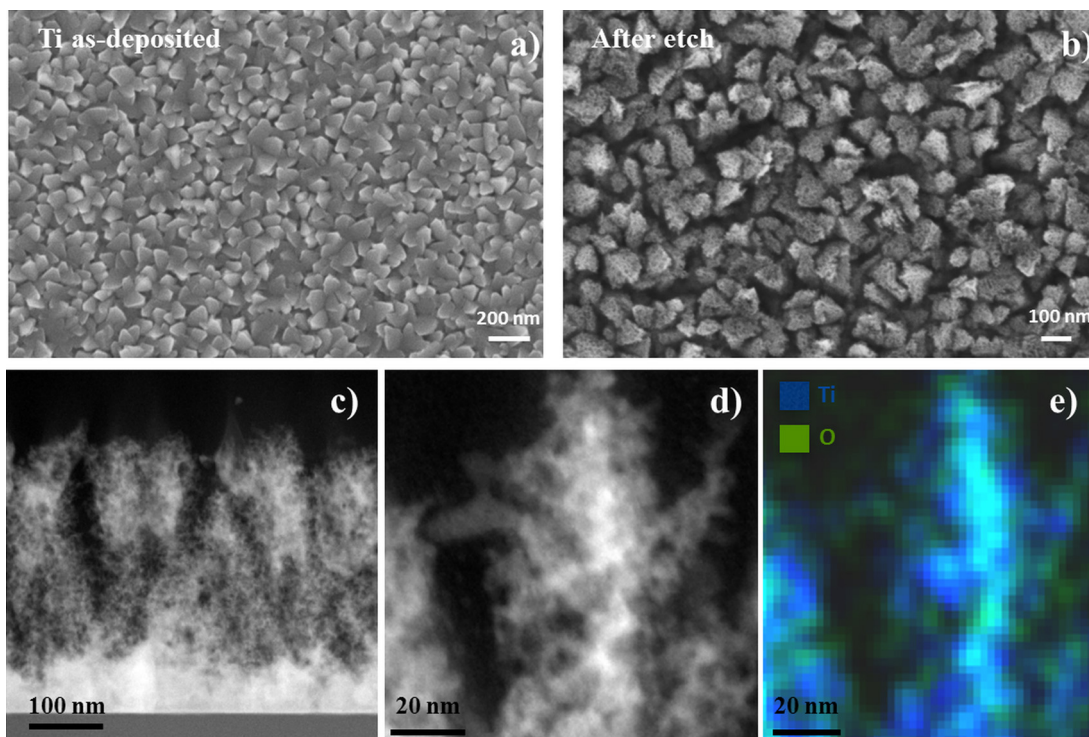
Fig. 1. Plan-view SEM images of Ti film as sputtered (a), and after the chemical etching in H_2O_2 (b). Cross-view TEM images of nanoplumes (c), a magnification of nanoplumes (d), and the chemical map (e), where blue and green pixels indicate titanium and oxygen atoms, respectively. (For interpretation of the references to color in this figure legend, the reader is referred to the web version of this article.)

localized than EDS, therefore it clearly shows where the chemical elements are located and here reveals a mixture of titanium (blue pixels) and oxygen (green pixels) into the plumes.

Fig. 2(a) shows the XRD spectra of sputtered Ti films (dotted line), after the chemical etching (short dotted line), after the chemical etching and subsequent thermal treatment at 400 °C (continuous line). Hereafter we will refer to these two last samples as "not annealed" and "annealed", respectively. Three peaks are clearly visible at 35–40° in the spectra of Ti film and not annealed samples, corresponding to metal titanium. This indicates that the etching did not completely erode the Ti film, as previously evidenced by STEM analyses (see Fig. 1(c)). A broad band at ~23°, with an asymmetric shape, is also visible. This band, already present in the Ti film, probably comes from the Ti-quartz interface. The annealing induced the suppression of Ti peaks, since the underneath Ti layer was fully transformed into TiO_2 due to the annealing in oxygen ambient. In addition, the spectrum of annealed sample clearly shows, differently from not annealed samples, the presence of two crystalline forms of titania: anatase and rutile (indicated with "A" and with "R", respectively, in Fig. 2(a)). A longer thermal treatment (2 h in oxygen at 400 °C) did not produced further variations in the crystalline structure of the nanoplumes.

In order to understand the possible presence and role of hydrogen (possibly coming from the etching process) we analyzed the synthesized nanoplumes by FTIR spectroscopy. The analyses are reported in Fig. 2(b). The not annealed and annealed samples show similar absorption features from $1000\,cm^{-1}$ to $6000\,cm^{-1}$, and both exhibit an absorption band at $\sim3700\,cm^{-1}$, due to the $v(O-H)$ stretching modes [28]. These results were compared to the FTIR spectra of TiO_2 flat films on quartz substrate, used as reference. Also a virgin quartz substrate was measured. These two latter samples do not show any absorption band at $\sim3700\,cm^{-1}$, emphasizing that the presence of OH groups observed in not annealed and annealed samples clearly originate from the etching process.

XPS analyses were performed and reported in Fig. 3. The continuous lines indicate the acquired spectra, dotted lines are the deconvolution of the peaks, red lines are the fits of the spectra, and grey lines are the subtracted baseline. In detail, the panels on the left side show the Ti 2p region for the TiO_2 flat films (Fig. 3(a)), not annealed samples (Fig. 3(c)), and annealed samples (Fig. 3(e)). All the analyzed samples present the typical Ti(IV) peaks, Ti $2p_{3/2}$ and Ti $2p_{1/2}$, located at 458.20 eV and 463.93 eV, respectively. In addition, not annealed and annealed samples show Ti(III) signal, Ti $2p_{3/2}$, at 456.65 eV. The Ti(III)/Ti(IV) ratio was calculated from the peak areas, and resulted to be ~5%, both in not annealed and annealed samples. The literature [19] reports that the presence of Ti(III) is an indirect evidence of the existence of oxygen vacancies, in order to maintain electrostatic balance. The panels on the right side of the figure report the O 1s region for the TiO_2 flat films (Fig. 3(b)), not annealed (Fig. 3(d)) and annealed samples (Fig. 3(f)). All the analyzed samples present the typical O 1s peaks due to the oxygen signals from the lattice (peaked at 531.05 eV), and from the hydroxyl groups (peaked at 529.9 eV). The percentage of hydroxyl groups was evaluated by the ratio between the area of OH and the total area of O 1s regions and resulted to be ~18% for both not annealed and annealed samples, while it resulted ~5% for TiO_2 films [29,30]. These results clearly indicate the presence of a significant amount of OH groups in the nanoplumes differently from what observed in flat films.

The UV–VIS diffused reflectance spectra were measured in the wavelength range of 250–1100 nm and they are shown in Fig. 4(a). Not annealed and annealed nanoplumes show a marked decrease of the reflectance for wavelength shorter than 800 nm compared to TiO_2 flat films. The oscillations of the spectra for both samples are due to optical effects of interference.

The absorbance (A) was obtained by the transmittance (T) and reflectance (R) measured spectra, in accordance to the following equation: $A\% = 100\% - T\% - R\%$, and it is reported in Fig. 4(b). The
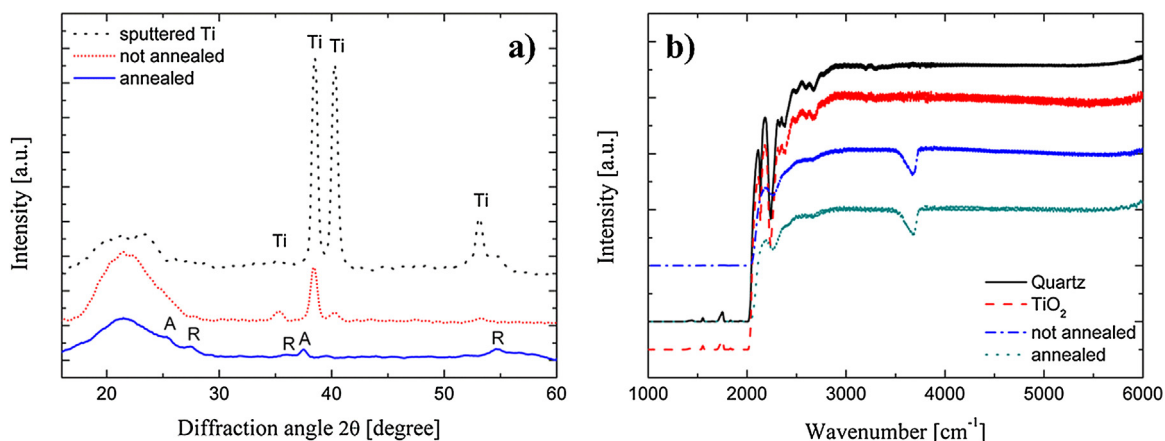
Fig. 2. (a) XRD patterns of sputtered Ti, not annealed (i.e. after the etching) and annealed (i.e. after the etching and the annealing) samples. (b) FTIR spectra of not annealed and annealed samples compared with a TiO_2 film and a quartz substrate.
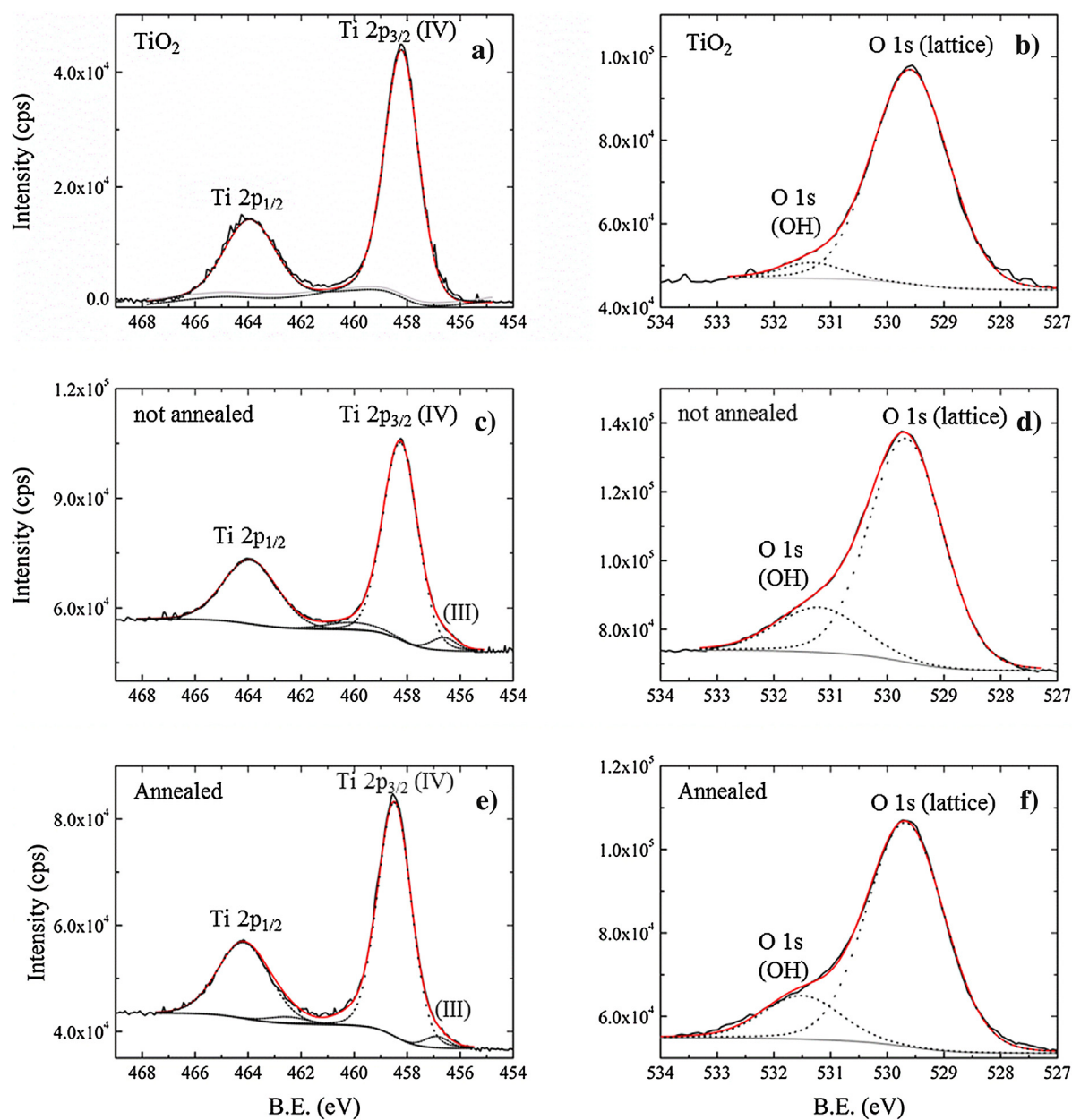

Fig. 3. Ti 2p XPS spectra of (a) TiO_2 film, (c) not annealed and (e) annealed sample. O 1s XPS spectra of (b) TiO_2 film, (d) not annealed and (f) annealed sample. Black continuous lines indicate the acquired spectra, dotted lines are the deconvolution of the peaks, red continuous lines are the fits of the spectra, and grey lines are the subtracted baselines.
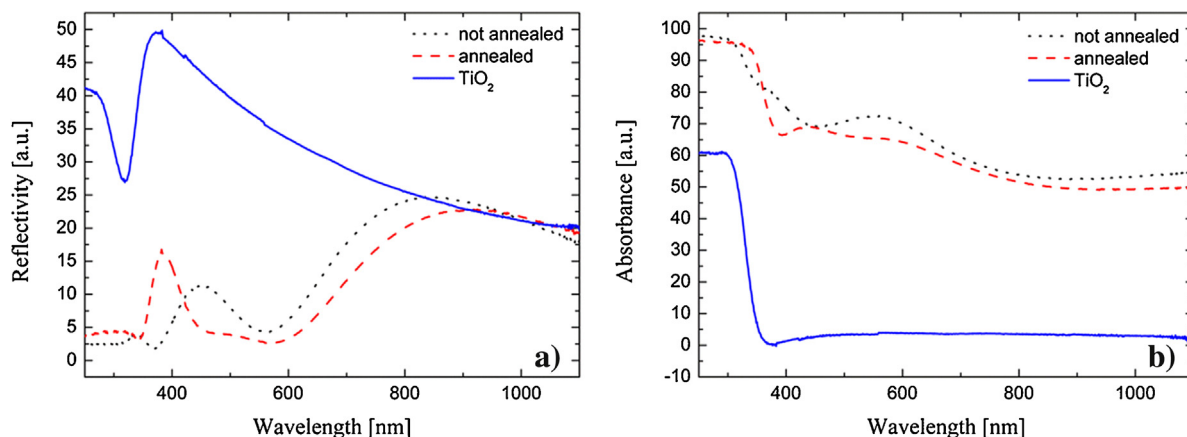
Fig. 4. (a) Reflectivity and (b) absorbance spectra of not annealed and annealed samples compared to a TiO$_2$ film.

results show that not annealed and annealed samples have a higher optical absorption in VIS and IR region (from 450 to 1100 nm), that is about 70% higher than the pure TiO$_2$. The enhanced absorbance in the visible is probably related to the presence of Ti^{3+} (evidenced by XPS analyses). Indeed, it is well known that Ti^{3+} introduce isolated states inside the forbidden energy gap. These isolated states have several energy levels, from 0.3 to 0.8 eV, below the minimum of the conduction band [31]. Starting from the optical absorption thresholds, we calculated the band-gap energy of the different materials [4]. The band-gap energy for TiO$_2$ flat films resulted ~3.2 eV (threshold wavelength at 387 nm), as expected [8]. Instead, not annealed and annealed samples have a band-gap energy of 2.1 eV (threshold wavelength at 592 nm) and 2.6 eV (threshold wavelength at 468 nm), respectively. These values were compared with the values obtained applying the Tauc model. This model is generally used to describe the light absorption process of amorphous semiconductors [32]. Following the Tauc model, for indirect transitions (that is the case of TiO$_2$ [33]) we obtained the following values: 3.2 eV for TiO$_2$ films, 2.4 eV for not annealed samples, and 2.7 eV for annealed samples. Assuming an error of 10% in the determination of the band-gap, the values estimated from the optical absorption thresholds are in good agreement with the values estimated by the Tauc model. Thus, both methods indicate that a band-gap narrowing was achieved by etching, suggesting that the chemical etching induced an important modification of the material, if compared with the titania flat films.

In order to check the photocatalytic activity of the nanoplumes in the degradation of organic compounds under UV and VIS light irradiation, we performed MB degradation measurements in water. The results were compared with that of TiO$_2$ flat films and sputtered Ti films. Fig. 5(a) and (b) report the logarithmic residual concentration of MB under UV and VIS light, respectively, versus the irradiation time. In particular, C is the concentration of MB after the irradiation, C_0 is the starting concentration of MB. We tested five samples: MB in absence of any catalyst materials (squares), MB with Ti sputtered film (diamonds), MB with TiO$_2$ flat film (stars), MB with not annealed sample (circles) and MB with annealed sample (triangles). Preconditioning process was applied to remove possible adsorbed organic pollutants on the surfaces (see materials and methods section). The samples were immersed in the MB solutions and kept in the dark more than one hour. This process allowed to evaluate the adsorption of MB on the different sample surfaces without involving any photocatalytic reaction. After the MB adsorption step, the samples were exposed to UV or VIS light, so to induce the photocatalysis. The observed reaction rate, k, follows a

Lagmuir–Hinshelwood model kinetics, which can be expressed by a first-order reaction:

$$\ln\left(\frac{C}{C_0}\right) = -kt$$

where C is the concentration of organic species, C_0 is the initial concentration of organic species, t is the irradiation time [34]. The reaction rates are reported in Fig. 5(a) and (b) for all the analyzed materials. The Ti films do not show any photocatalytic properties, as expected. In both irradiation conditions the nanostructured samples exhibit a considerable enhancement of the photocalytic activities. This is rationally due to the high exposed surface, but also to the multiple scattering events of the light passing through the nanoplumes, thus increasing the absorption of the light. Furthermore the higher amount of OH groups increases the photocatalytic activity. Indeed, in a photocatalytic process the first stage of the process involves the direct interaction between the dye and the surface of the sample. In detail, the MB molecules can adhere to the TiO$_2$ surface thanks to the electrostatic attraction between=N(CH$_3$)$_2$$^+$ and OH$^-$ groups. Then, a higher concentration of OH$^-$ groups can be responsible for a higher adhesion of MB molecules on the TiO$_2$ surface [35]. The best photocatalytic activity under UV light irradiation was shown by annealed samples (with a reaction rate, k, 5 times the rate of TiO$_2$ films). This is due to the complete oxidation of the Ti film at the bottom of the nanoplumes induced by the thermal process (as confirmed by the XRD analyses, see Fig. 2(a)).

Under VIS light irradiation not annealed samples show the highest photo-degradation reaction rate (~5 times the rate of TiO$_2$ films). This result can be correlated to: (1) the generated structural defects, and to (2) the Ti underneath layer. (1) For dielectric films in presence of H atoms or large amount of lattice disorder, the disappearance of medium- and long-range order causes a considerable blurring of the edges of the conduction and valence bands, as well as gives rise to a distribution of deep levels in the forbidden gap [36]. As a consequence we hypothesize that the generated structural defects in our material are responsible for the observed band-gap narrowing for not annealed and annealed samples (see Fig. 4(b)). But, the subsequent thermal treatment of nanoplumes (annealed samples), induces a crystallization (Fig. 2(a)). The annihilation of defects causes an enlargement of the energy gap, as confirmed by the absorbance spectra (see Fig. 4(b)). This is clearly the reason for the observed reduction of the photocatalytic activity under the VIS light. (2) Another contribution to the high photocatalytic efficiency under VIS irradiation could be given by the residual Ti film placed at the bottom of the nanoplumes. In fact, simulations carried out with SCATMECH code showed that metal Ti acts as an
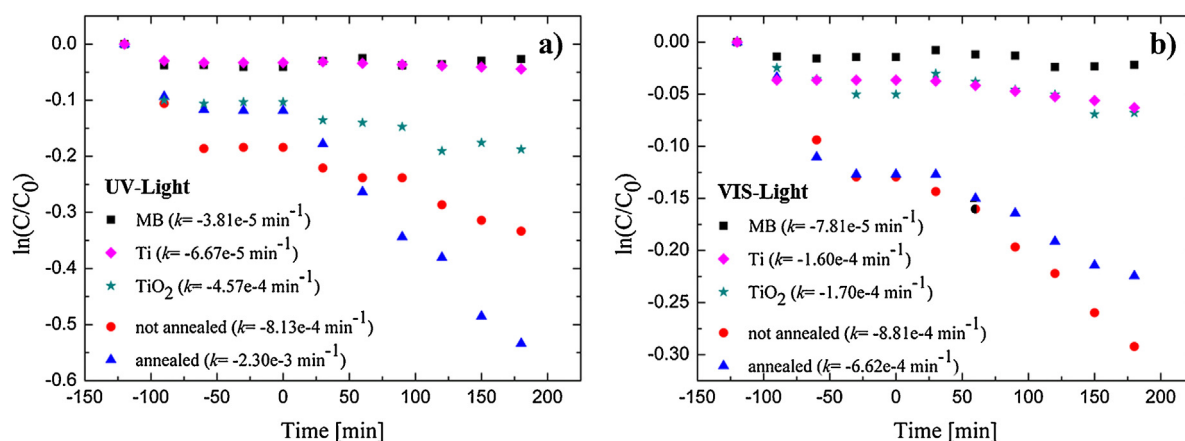
Fig. 5. MB degradation under (a) UV and (b) VIS light for five samples: MB (squares), MB with Ti sputtered film (diamonds), MB with TiO₂ film (stars), MB with not annealed sample (circles), MB with annealed sample (triangles).

efficient reflective layer, in an ideal scenario of 70 nm of metallic Ti under 300 nm of crystalline TiO₂ [37]. In the present case, the top layer of nanoplumes can absorb these reflected photons more efficiently than a flat TiO₂ film. The annealing process is responsible for a complete oxidation of the residual underneath Ti layer into TiO₂ (as confirmed by XRD analyses). The oxidation of the Ti layer in the TiO₂ turns the layer transparent to the light. Thus it loses its reflective properties and its energy gap cannot be excited by the VIS radiation.

After the photocatalytic tests the samples were again characterized by SEM and XPS analyses, in order to verify the stability of the synthesized material. Here, we report the results for not annealed samples. SEM analysis, shown in Fig. 6, did not revealed any modification of the nanostructure. XPS analysis reported in Fig. 7 shows the same percentage of Ti(III)/Ti(IV), i.e. ∼5%, and the same percentage of hydroxyl groups (evaluated by the ratio between the area of OH and the total area of O 1s regions), i.e. ∼18%, as previously detected (see Fig. 3). A small band at ∼533 eV in the O 1s region can be now detected (Fig. 7(b)). This band is due to OH groups related to water remains, caused by the cleaning steps after the discoloration measurements [38].

Considering that not annealed samples showed the best efficiency in degrading MB under VIS light irradiation, the antibacterial activity was tested using the same VIS irradiation conditions as in photocatalysis experiment. E. coli ATCC25922 was chosen as a model organism. This strain is mostly used in tests aimed at testing food safety and it is not genetically modified for molecular biology purposes. Thus, the possible resistance mechanisms of the bacteria
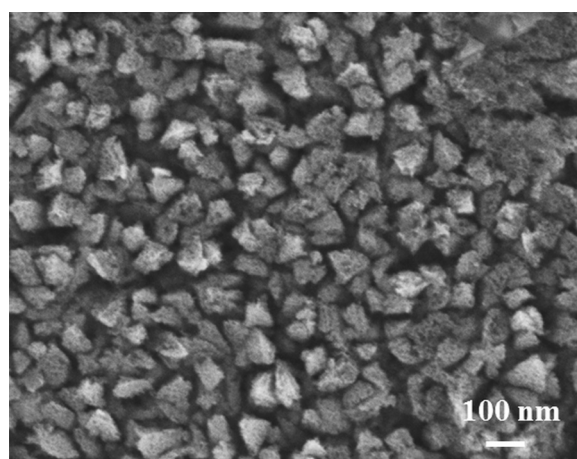

Fig. 6. Plan-view SEM image of the nanoplumes after the MB tests.

were not weakened. Furthermore, E.coli has been recently recognized as a more reliable indicator of fecal contamination in drinking water and other matrices [39]. The survival rate of E. coli ATCC25922 was measured after 15′ and 60′ exposure to the samples under VIS source. Untreated and exposed to VIS only samples were run in parallel as controls. Results were normalized toward initial bacterial concentration and the statistical error of the test is 5%. As shown in Fig. 8, after one hour of exposure under VIS light, bacterial survival dropped down to 17% for the not annealed samples, while it
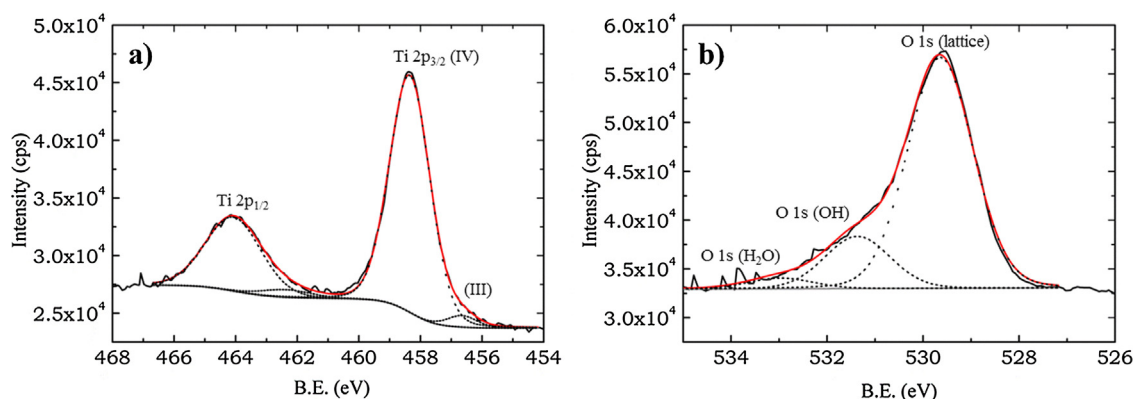

Fig. 7. Ti 2p (a) and O1s (b) XPS spectra of not annealed sample after MB tests. Black continuous lines indicate the acquired spectra, dotted lines are the deconvolution of the peaks, red continuous lines are the fits of the spectra, and gray lines are the subtracted baselines.
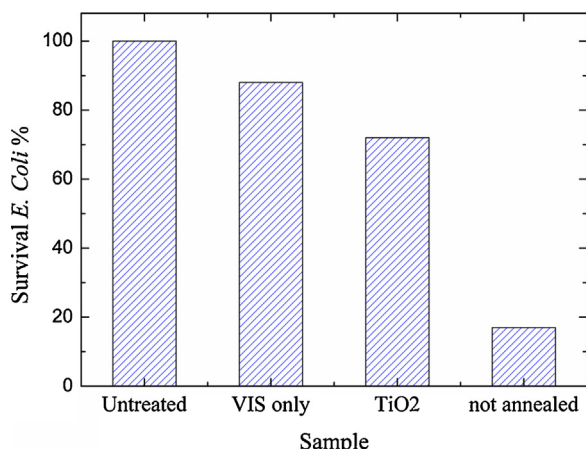
Fig. 8. Antibacterial activity test. Relative *E. coli* survival rate for CFU count after 60 min exposure to TiO_2 and nanoplumes (not annealed) under VIS light irradiation. Untreated control and VIS control were run in parallel.

dropped down only to 72% for the TiO_2 flat films. Exposure of *E. coli* to VIS light in the absence of TiO_2 reduced the bacteria survival percentage only to 88%, thus damage due to VIS light only was modest [40]. Therefore, the major reason for the antibacterial effect was due to the presence of the nanoplumes, that can be activated by VIS light. In fact, it is generally accepted that TiO_2 based nanomaterials show an antibacterial effect through a mechanism of oxidative stress due to reactive oxygen species (ROS) that are generated in the UV/TiO_2 process in an aqueous environment [41]. However, VIS source is not sufficient to trigger this process in presence of the TiO_2 flat film, due to the low capability of the material to absorb the light in this region and then to generate ROS.

4. Conclusions

In summary, black TiO_2 nanoplumes were synthesized by a straightforward method, involving a rapid chemical etching in a H_2O_2 solution. The high exposed surface area together with the high concentration of OH groups and the generated structural defects are responsible for the high photocatalytic properties under UV–VIS light irradiation, with a reaction rate about 5 times than TiO_2 films. The thermal annealing process modulates the properties of nanoplumes. The reported results show that the synthesized nanoplumes have a significant efficiency in degrading methylene blue organic compound and a good antibacterial activity under VIS light irradiation. The presented synthesis process may be applied for the fabrication of efficient hydrogenated photocatalytic materials as an alternative to high temperature and high pressure approaches. In addition, the proposed method is industrially scalable, with relatively low cost, and with no environmental impact.

Acknowledgments

References

[1] M. Grätzel, Inorg. Chem. 44 (2005) 6841–6851.
[2] M. Wagemaker, A.P.M. Kentgens, F.M. Mulder, Nature 418 (2002) 397–399.
[3] A. Fujishima, K. Honda, Nature 238 (1972) 37–38.
[4] S.U.M. Khan, M. Al-Shahry, W.B. Ingler Jr., Science 27 (2002) 2243–2245.
[5] R. Wang, K. Hashimoto, A. Fujishima, M. Chikuni, E. Kojima, A. Kitamura, M. Shimohigoshi, T. Watanabe, Nature 388 (1997) 431–432.
[6] X. Chen, S.S. Mao, Chem. Rev. 107 (2007) 2891–2959.
[7] M.A. Shannon, P.W. Bohn, M. Elimelech, J.G. Georgiadis, B.J. Marinas, A.M. Mayes, Nature 452 (2008) 301–310.
[8] A. Bendavid, P.J. Martin, A. Jamting, H. Takikawa, Thin Solid Films 355 (1999) 6–11.
[9] V. Scuderi, G. Impellizzeri, L. Romano, M. Scuderi, M.V. Brundo, K. Bergum, M. Zimbone, R. Sanz, M.A. Buccheri, F. Simone, G. Nicotra, B.G. Svensson, M.G. Grimaldi, V. Privitera, Nanoscale 6 (2014) 11189–11195.
[10] V. Subramanian, E.E. Wolf, P.V.J. Kamat, Am. Chem. Soc. 126 (2004) 4943–4950.
[11] V. Scuderi, G. Impellizzeri, L. Romano, M. Scuderi, G. Nicotra, K. Bergum, A. Irrera, B.G. Svensson, V. Privitera, Nanoscale Res. Lett. 9 (2014) 458–465.
[12] D.V. Bavykin, F.C. Walsh, Titanate and Titania Nanotubes: Synthesis, Properties and Applications, Royal Society of Chemistry Nanoscience and Nanotechnology Monograph, 2009, ISBN: 978-1-84755-910-4.
[13] S. Malato, P. Fernàndez-Ibáñez, M.I. Maldonado, J. Blanco, W. Gernjak, Catal. Today 147 (2009) 1–59.
[14] G. Impellizzeri, V. Scuderi, L. Romano, E. Napolitani, R. Sanz, R. Carles, V. Privitera, J. Appl. Phys. 117 (2015) 105308.
[15] X. Chen, L. Liu, P.Y. Yu, S.S. Mao, Science 331 (2011) 746–750.
[16] G. Wang, H. Wang, Y. Ling, Y. Tang, X. Yang, R.C. Fitzmorris, C. Wang, J.Z. Zhang, Y. Li, Nano Lett. 11 (2011) 3026–3033.
[17] Z. Zhang, M. Bai, D. Guo, S. Hou, G. Zhang, Chem. Commun. 47 (2011) 8439–8441.
[18] Z. Zheng, B. Huang, J. Lu, Z. Wang, X. Qin, X. Zhang, Y. Dai, M. Whangbo, Chem. Commun. 48 (2012) 5733–5735.
[19] X. Jiang, Y. Zhang, J. Jiang, Y. Rong, Y. Wang, Y. Wu, C. Pan, J. Phys. Chem. C 116 (2012) 22619–22624.
[20] N. Liu, C. Schneider, D. Freitag, M. Hartmann, U. Venkatesan, J. Müller, E. Spiecker, P. Schmuki, Nano Lett. 14 (2014) 3309–3313.
[21] J.-M. Wu, J. Crystal Growth 269 (2004) 347–355.
[22] Z.-Y. Chen, Y. Hua, T.-C. Liu, C.-L. Huang, T.-S. Jeng, Thin Solid Films 517 (2009) 4998–5000.
[23] P. Tengvall, H. Elwing, I. Lundstrom, J. Colloid Interface Sci. 130 (1988) 405–413.
[24] M.R. Ayers, A.J. Hunt, Mater. Lett. 34 (1998) 290–293.
[25] Q.X. Liu, et al., Eur. Phys. J. B 41 (2004) 479.
[26] G. Nicotra, Q.M. Ramasse, I. Deretzis, A. La Magna, C. Spinella, F. Giannazzo, ACS Nano 7 (2013) 3045–3052.
[27] R. Wang, K. Hashimoto, A. Fujishima, M. Chikuni, E. Kojima, A. Kitamura, T. Watanabe, Nature 388 (1997) 431–432.
[28] K. Nakamura, K. Ueda, S. Sato, Langmuir 17 (2001) 2298–2300.
[29] B. Erdem, R.A. Hunsicker, G.W. Simmons, E.D. Sudol, V.L. Dimonie, M.S. El-Aasser, Langmuir 17 (2001) 2664–2669.
[30] M.C. Biesinger, L.W.M. Lau, A.R. Gerson, R. St, C. Smart, Appl. Surf. Sci. 257 (2010) 887–898.
[31] M. Liu, X. Qiu, M. Miyauchi, K. Hashimoto, Chem. Mater. 23 (2011) 5282–5286.
[32] J. Tauc, Amorphous and Liquid Semiconductors, Plenum, New York, 1974, pp. 175.
[33] G. Impellizzeri, V. Scuderi, L. Romano, P.M. Sberna, E. Arcadipane, R. Sanz, M. Scuderi, G. Nicotra, M. Bayle, R. Carles, F. Simone, V. Privitera, J. Appl. Phys. 116 (2014), 173507-1-8.
[34] M.N. Chong, B. Jin, C.W.K. Chow, C. Saint, Water Res. 44 (2010) 2997–3027.
[35] B. Liu, L. Wen, K. Nakata, X. Zhao, S. Liu, T. Ochiai, T. Murakami, A. Fujishima, Chem. Eur. J. 18 (2012) 12705–12711.
[36] A.K. Jonscher, Thin Solid Films 1 (1967) 213–234.
[37] http://pml.nist.gov/Scatmech/html/index.htm.
[38] H.Y. Chung, S.H. Lee, T.W. Kim, J. Electrochem. Soc. 159 (2012) 771–774.
[39] S.T. Odonkor, J.K. Ampofo, *Escherichia coli* as an indicator of bacteriological quality of water: an overview, Microbiol. Res. 4 (2013), N1.
[40] R. Lubart, A. Lipouski, Y. Nitzan, H. Friedmann, Laser Ther. 20 (2011) 17–22.
[41] M. Cho, H. Chung, W. Choi, J. Yoon, Water Res. 38 (2004) 1069–1077.